International Journal of Heat and Mass Transfer 136 (2019) 170–177

Contents lists available at ScienceDirect

International Journal of Heat and Mass Transfer

journal homepage: www.elsevier.com/locate/ijhmt

Simultaneous prediction of dryout heat flux and local temperature for thin film evaporation in micropillar wicks

Geoffrey Vaartstra, Zhengmao Lu, Evelyn N. Wang *

Department of Mechanical Engineering, Massachusetts Institute of Technology, Cambridge, MA 02139, USA

ARTICLE INFO

Article history:
Received 16 November 2018
Received in revised form 22 February 2019
Accepted 22 February 2019

ABSTRACT

Porous wicks are of great interest in thermal management because they are capable of passively supplying liquid for thin film evaporation, a promising method to reliably dissipate heat in high performance electronics. While dryout heat flux has been well-characterized for many wick configurations, key design information is missing as many previous models cannot determine the distribution of evaporator surface temperature. Temperature gradients are inherent to the passive capillary pumping mechanism since the shape of the liquid/vapor interface is a function of the local liquid pressure, causing spatial variation of permeability and heat transfer coefficient (HTC). Here, we present a comprehensive modeling framework for thin film evaporation in micropillar wicks that can predict dryout heat flux and local temperature simultaneously. Our numerical approach captures the effect of varying interfacial curvature across the micropillar evaporator to determine the spatial distributions of temperature and heat flux. Heat transfer and capillary flow in the wick are coupled in a computationally efficient manner via incorporation of parametric studies to relate geometry and interface shape to local permeability and HTC. This model predicts notable variations of HTC (~30%) across the micropillar wick, highlighting the significant effects of interfacial curvature. Further, we are able to quantify the tradeoff associated with enhancing either dryout heat flux or HTC by optimizing geometry. Our model provides all of the information needed to guide the design and optimization of micropillar wicks by resolving evaporator temperature distributions in addition to dryout heat flux.

1. Introduction

As emerging technology continues to produce high performance, high power density electronics, heat dissipation becomes an increasingly critical challenge [1–4]. Liquid-vapor phase change has garnered much interest as a thermal management strategy since the latent heat of vaporization allows for high-flux heat removal. While flow boiling in microchannels has been broadly researched [5–7], flow instabilities and a high pumping power requirement have led to a separate focus on thin film evaporation from porous wicks [8–10]. This approach offers the advantages of passive, capillary-driven flow and a high heat transfer coefficient (HTC) due to low thermal resistance of the thin (<100 μm) liquid film. Consequently, use of porous wicks has become widespread in heat pipes and vapor chambers to cool electronics [3]. These devices take advantage of low resistance vapor transport to act as very effective heat spreaders [11], yet improvements in evaporator wick performance remain an active area of research.

To obtain fundamental insights, wicks with well-defined structures are ideal. Such precise control over geometric parameters can be achieved using traditional silicon nanofabrication techniques to create wicks comprised of arrays of micropillars. These micropillar wicks have been extensively studied [12–18] since they can be tailored and optimized using well-characterized fabrication processes. Previous work has primarily been focused on predicting the maximum heat flux a wick can sustain, typically referred to as the dryout heat flux. Models to predict dryout heat flux [12,14] have been developed based on studies of fluid flow in micropillar wicks [17,19]. These models serve as design guidelines to optimize geometry for permeability and capillary pressure, both of which influence dryout. Adera et al. [12] approximated permeability as uniform [17] and used Brinkman's Equations [20] coupled with uniform evaporative mass loss to calculate dryout heat flux. Zhu et al. [14] captured the effects of the varying liquid-vapor interface shape by solving the 3D meniscus profile and performing computational fluid dynamics (CFD) simulations to determine permeability. Pressure and velocity distributions were then solved numerically for uniform evaporation over the micropillar wick to predict dryout heat flux.

* Corresponding author.
E-mail address: enwang@mit.edu (E.N. Wang).

https://doi.org/10.1016/j.ijheatmasstransfer.2019.02.074
0017-9310/

Although these works have been able to accurately model the effects of micropillar geometry and wicking length on dryout heat flux, the HTC has not been rigorously characterized. Recently, Wei et al. [18] addressed micropillar optimization for both dryout heat flux and superheat by determining an effective thermal conductivity from finite element calculations for a flat interface. Extending that approach, Somasundaram et al. [21] solved for the meniscus shape and effective thermal conductivity using a finite element solver and modeling interfacial heat transfer with Schrage's equation [22]. However, these works did not combine the HTC with a fluid model that incorporated the variation of interface shape across the evaporator wick, which can lead to inaccuracies in the modeling results. Therefore, a combined fluid and heat transfer model that resolves distributions of interface shape, HTC, and temperature has yet to be demonstrated.

In this work, we have formulated a framework to comprehensively model thin film evaporation in micropillar wicks based on three principal design criteria: source temperature (T_s), evaporator temperature (T_e), and dryout heat flux (q''_{dryout}). In practical applications, source temperature is constrained by the operating limit of the electronics, while evaporator temperature is constrained by the boiling limit to avoid undesired nucleation [11]. Dryout heat flux is defined as the operating point at which the working fluid evaporates from the wick faster than it can be replenished. Under specified working conditions, the temperature at the evaporator surface is directly dependent on the HTC, and source temperature can be extrapolated by considering conduction in the substrate. Therefore, all three design criteria can be addressed by determining HTC and dryout heat flux for a given porous wick. Further, the variation of HTC on the evaporator due to liquid-vapor interface shape must be considered: our model shows that HTC varied by ~30% on a 1 cm × 1 cm micropillar wick under specific operating conditions. However, considering the distribution of HTC amongst micron scale features on a millimeter scale wick presents a challenge for computational efficiency. Our framework consists of performing parametric studies of single micropillar cells and incorporating those results into a device-level model. In this manner, the microstructure is not directly simulated, yet rather is lumped into a set of pressure dependent properties. This efficient method is capable of resolving distributions of pressure and temperature on the wick, as well as predicting dryout heat flux, thus addressing all three evaporator design criteria. Since the modeling framework used here is valid for any wick with a periodic structure, its potential impacts extend beyond thin film evaporation in micropillar wicks.

2. Model formulation

An input heat flux (q''_{in}) is applied to a micropillar wick of wicking length L (edge to center of device) and is dissipated via thin film evaporation ($q''_e(x)$) into pure vapor (Fig. 1). Capillary forces wick liquid into the micropillar array from the supply at the saturation temperature (T_{sat}), thus passively maintaining a wetted surface. The micropillar array treated here is comprised of a square unit cell (Fig. 1(b)) repeated in a periodic fashion and defined by its diameter (d), pitch (l), and height (h). Due to the capillary pressure gradient across the substrate that drives flow, the liquid-vapor interface shape varies from cell to cell. The local interface shape can be described by its mean curvature (H), which is related to the capillary pressure ($\Delta p = p - p_0$) according to the Young-Laplace Equation (Eq. (1)) where σ is the liquid-vapor surface tension.

$$\Delta p = 2\sigma H. \tag{1}$$

This relation applies to all cases presented here as the Bond number is small ($Bo = \Delta\rho g l^2/\sigma \sim 10^{-5}$, see *A.1.* for characteristic values used to determine dimensionless parameters).

Accounting for local effects of interface shape on heat transfer and capillary flow is crucial to this model. To accomplish this, we conducted parametric studies to determine the evaporative heat transfer coefficient (h_e) and local permeability (κ) of the wick over a range of micropillar geometries and interfacial curvatures. Throughout this study, we considered water as the working fluid and silicon as the micropillar material. The key assumptions behind this model are that convection in the thin film is negligible, lateral conduction in the fluid is much smaller than conduction towards the interface, the variation of curvature within a unit cell can be neglected, and evaporation is near equilibrium (see *A.1.* for validation of these assumptions).

2.1. Interface shape

When operating below the dryout limit, the three phase contact line is pinned to the top of the pillars and forms a meniscus. We solved for the 3D meniscus profile using a method identical to those used by [14,23]. The shape of the capillary surface ($F = f(x,y) - z$) can be determined by differential geometry [24], which relates the outward unit normal vector ($\hat{n} = \nabla F/|\nabla F||$) of the interface to its mean curvature. By this method, the interface is described by a static normal stress balance (Eq. (2)), where H is defined as positive when the liquid surface is convex, effects of gravity and inertial perturbation are neglected, and curvature is approximated as constant over the unit cell (see *A.1.*).

$$\nabla \cdot \hat{n} = 2H. \tag{2}$$

This nonlinear differential equation was solved in COMSOL Multiphysics [25] on the domain shown in Fig. 2(a) by imposing $z = 0$ at the pillar edges and symmetry at the cell boundaries (all mesh convergence details can be found in *A.2.*). Once resolved, the interface shape was imported as a mesh into the heat transfer and fluid parametric studies. For each parametric study, the maximum curvature corresponded to the dryout capillary pressure (Δp_{dryout}) as determined by a force balance at the contact line when the receding contact angle (θ_{rec}) is formed (Eq. (3)).

$$\Delta p_{dryout} = \frac{4\sigma\cos\theta_{rec}}{d\left(\frac{4}{\pi}\left(\frac{l}{d}\right)^2 - 1\right)} \tag{3}$$

2.2. Parametric studies

Modeling physics in microscale features on a millimeter scale wick entails an inherent tradeoff between computational efficiency and accuracy. We have approached this problem by parametrically studying the evaporative heat transfer coefficient and permeability of single micropillar cells as functions of geometry and capillary pressure (interface shape). These studies produced lookup tables for the device-level model that allow the wick to be modeled as a flat surface with pressure dependent properties.

The parametric study of heat transfer was conducted by determining h_e (Eq. (4)) for a known q''_{in} being rejected to a pure vapor ambient at T_{sat} where the average evaporator temperature (T_e) was solved by a finite element calculation (Fig. 2(b)).

$$h_e = \frac{q''_{in}}{T_e - T_{sat}} \tag{4}$$

In the computational domain, a uniform heat flux is supplied to the bottom of the cell, 1 μm below the base of the pillars to account for constriction resistance. Since symmetry conditions are enforced at the lateral boundaries of the cell (see *A.1.*), heat is dissipated from the unit cell solely by evaporation from the liquid-vapor interface (q''_e). Natural convection from the tops of the silicon pillars is

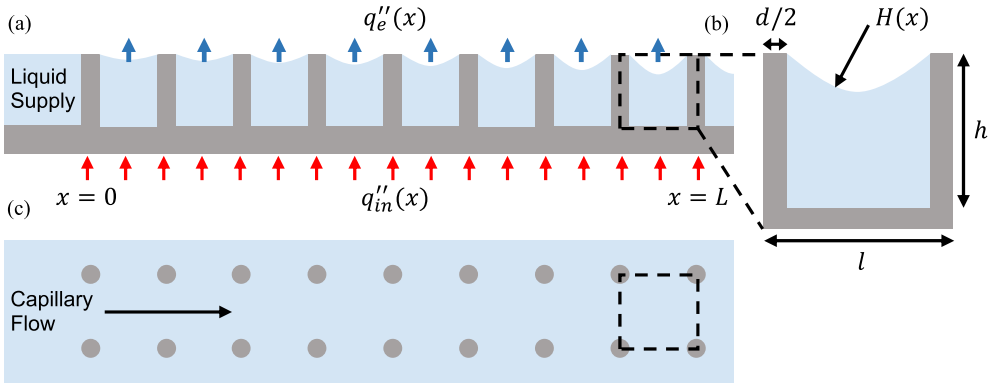

Fig. 1. (a) Side view schematic of a micropillar wick operating during thin film evaporation. An input heat flux q_{in}'' is applied to the bottom of the substrate and is rejected by evaporation into pure vapor. Capillary pressure maintains a wetted surface by passively pumping liquid from the supply ($x = 0$) to the center of the device ($x = L$). (b) Schematic of a micropillar cell, which can be defined by its geometry (d, l, h) and the local mean curvature of the liquid-vapor interface ($H(x)$). (c) Top view of the micropillar wick. Net flow is along the x coordinate only in the case where the liquid supply contacts only the sides of the wick normal to the x axis.

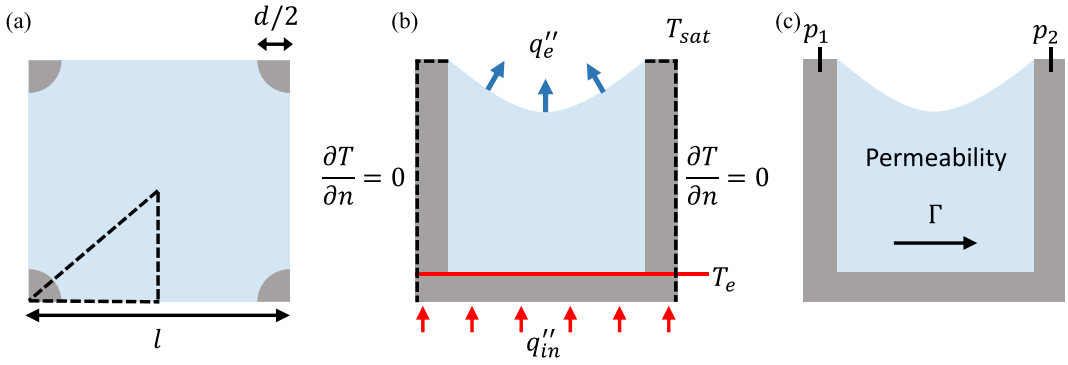

Fig. 2. (a) Top view showing the lines of symmetry of the micropillar unit cell. Only the region enclosed by the dashed lines is treated as the domain. (b) Side view depicting the heat transfer parametric study where heat from q_{in}'' is dissipated solely via evaporation. Symmetry (insulated) boundary conditions are applied to the lateral faces and pillar tops. The temperature of the evaporator (T_e) is evaluated as the average temperature at the surface (red line). (c) Side view depicting the flow parametric study. Mass flux due to an imposed pressure drop is reported in order to calculate the permeability from Darcy's Law. The interface is set as a symmetry boundary to impose no flux and no shear stress.

neglected as the thermal resistance to natural convection was estimated to be 3 orders of magnitude higher than thermal resistance to evaporation (see *A.1.*).

We calculate $q_e''(T_l)$, where T_l is the temperature of liquid at the interface, using a solution to the linearized Boltzmann Transport Equation (BTE) for Boltzmann-Krook-Welander molecules (Eqs. (5) and (6))

$$\frac{p_k}{p_l} - 1 = \frac{c_4^* u_k}{(2RT_l)^{1/2}} \tag{5}$$

$$\frac{T_k}{T_l} - 1 = \frac{d_4^* u_k}{(2RT_l)^{1/2}} \tag{6}$$

where the coefficients are given as $c_4^* = -2.13204$ and $d_4^* = -0.44675$ [26], R is the specific gas constant, and the subscript "k" indicates a variable evaluated at the Knudsen layer boundary. Low Mach number (near equilibrium) evaporation is an implicit restriction when using the linearized BTE (see *A.1.*). After additionally constraining the pressure at the Knudsen layer boundary to equal the far field pressure, the evaporative heat flux can be expressed as a function of the mean vapor speed at the Knudsen layer (Eq. (7)).

$$q_e'' = \rho_k u_k h_{lv}. \tag{7}$$

The accommodation coefficient for evaporation/condensation [27] was chosen as $\alpha = 0.052$ to match data from Adera et al. [12] and was accounted for using the method outlined by Meland and Ytrehus [28]. We solved this steady state problem using COMSOL Multiphysics for numerous geometries at capillary pressures ranging from zero to Δp_{dryout}.

A parametric study of laminar flow in micropillar cells was conducted by adapting the methods of Zhu et al. [14]. In summary, the Navier-Stokes Equations were solved in COMSOL for laminar flow (Reynolds number $Re_h = \rho u h/\mu \sim 10^1$) over a range of geometries and interfacial curvatures. A pressure difference was imposed across the cell and the mass flux (Γ) was reported (Fig. 2(c)), from which the Darcian permeability (κ) could be back calculated from Darcy's Law (Eq. (8)) where μ is the dynamic viscosity of the liquid.

$$\boldsymbol{u} = -\frac{\kappa}{\mu}\nabla p. \tag{8}$$

For a fixed geometry, permeability is a function of interface shape only, which is set by the local capillary pressure. More pronounced curvature yields lower permeability since the effective cross section of the flow is reduced. The effect of curvature was accounted for by importing the corresponding interface shape and setting it as a symmetry boundary, which enforces no flux and no shear stress at the interface. By this method, a look up table for permeability as a function of geometry and capillary pressure was compiled.

2.3. Device-level model

We formulated a device-level model for micropillar wicks by coupling fluid and conduction domains for an arbitrary heat load (see *A.4.* for a non-uniform heat load example) into a substrate of

thickness t_s. The fluid domain is considered as a continuous, porous medium modeled by Darcy's Law. Given a wick of uniform geometry, the permeability is a function only of local pressure as described by the parametric study. Reference pressure is set at the inlet while $x = L$ is a symmetry boundary. Due to the low speed of liquid moving toward the interface (Peclet number $Pe_h = u_e h\rho c_p/k \sim 10^{-2}$, see *A.1.*), evaporation could be modeled as a volumetric mass loss (Eq. (9))

$$\nabla \cdot (\rho \boldsymbol{u}) = Q_m, \tag{9}$$

where $Q_m = -q_e''(x)/(h_{lv}h)$.

The conduction domain takes an arbitrary heat flux input that is dissipated from the evaporator surface according to $q_e''(x) = h_e(x)\Delta T$, where $h_e(x)$ is a function of the local pressure solved in the fluid domain according to the parametric study ($h_e(x) = f(\Delta p(x))$) and ΔT is the local superheat ($T - T_{sat}$). $q_e''(x)$ is then returned to the fluid domain for the next iteration such that the distribution of evaporative heat flux is accounted for in the pressure calculation. In this way, the fluid and conduction domains are coupled by passing pressure and heat flux distributions, respectively (see *A.3.* for visual reference). For all device simulations presented in this work, this process was iterated until the Euclidean norms of the pressure and heat flux distributions each converged to a relative tolerance of at most 10^{-6}. Symmetry boundaries were assigned to $x = 0$ and $x = L$, which is reasonable so long as liquid is supplied at T_{sat}.

3. Results and discussion

3.1. Heat transfer coefficient

Beyond allowing for accurate modeling of micropillar wick performance, the parametric study of heat transfer shows the effects of geometry and local pressure on the evaporative heat transfer coefficient. We present two studies of evaporation into pure water vapor at 100 °C that highlight these effects: varying l while holding constant d = 10 μm and h = 25 μm (Fig. 3(a)); and varying h while holding constant d = 10 μm and l = 30 μm (Fig. 3(b)). q_{in}'' was set to 50 W/cm^2 for both parametric sweeps in Fig. 3. For each geometry, h_e was determined for Δp ranging from zero (flat interface) to the Δp_{dryout} corresponding to θ_{rec} = 15° (receding contact angle for water on silicon dioxide [29]). We observed that for a fixed geometry, h_e increased with capillary pressure. As interfacial curvature becomes more pronounced, the effective thickness of the evaporating film decreases, thus lowering the conduction resistance of the liquid. In addition, the augmented interfacial area additionally enhances the evaporation rate. For increasing pillar height, h_e dropped steadily since film thickness scales with h, effectively increasing conduction resistance (Fig. 3(b)). It can be seen that the effect of curvature was dampened for tall pillars, i.e., less variation of h_e across a wick will be observed for larger values of h/d. Dependence of h_e on the input heat flux is weak for this representative geometry (Fig. 3(a)): a 10% change of q_{in}'' resulted in a 0.082% average difference in predicted h_e.

3.2. Device simulation

Results of the device-level model for a single set of conditions are shown in Fig. 4, where d = 10 μm, l = 30 μm, h = 25 μm, L = 5 mm, t_s = 100 μm, and the ambient was pure water vapor at T_{sat} = 100 °C. These chip dimensions are standard and the micropillar geometry was shown to be near-optimal for dryout [14] with a large HTC (h_e > 60 kW/m^2 K). We prescribed a uniform input heat flux q_{in}'' = 82 W/cm^2, which is the dryout heat flux for the given set of geometry and operating conditions. For simplicity, this micropillar wick was considered to contact the liquid supply only at the two edges normal to the x axis (Fig. 1(c)), reducing the distributions to one dimension. Our model was able to resolve the distributions of evaporator (ΔT_e) and source (ΔT_s) superheats (Fig. 4(a)), as well as capillary pressure and heat transfer coefficient (Fig. 4(b)). While Δp was determined by the finite element solver, h_e was calculated directly from Δp via the lookup table from the parametric study, thus making this device-level model computationally feasible. Given that heat transfer is enhanced by curvature, h_e was highest near the center of the device ($x/L = 1$) where Δp reached a minimum. Under these specific conditions, h_e varied by ~30% across the micropillar wick. It follows that the superheat reached a minimum at the center and was the highest at the edge of the wick: in this simulation, we observed a ~3 °C difference in surface temperature, meaning that the inlet is more susceptible to boiling. The source and evaporator temperature design criteria can be addressed because the model predicts the maximum temperatures and their locations.

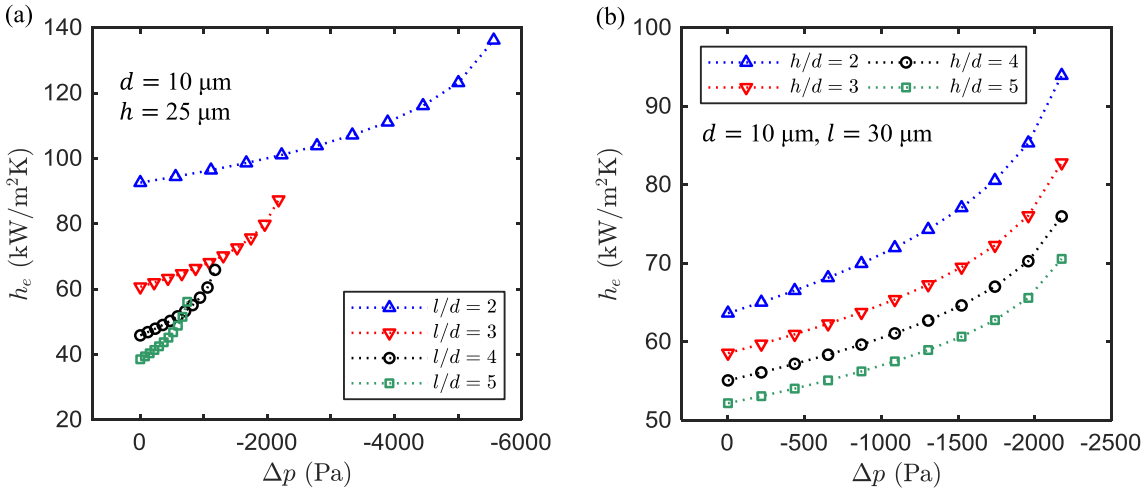

Fig. 3. (a) Parametric sweep of pitch and capillary pressure, with $d = 10$ μm and $h = 25$ μm constant. h_e increased with capillary pressure and was higher on average for smaller pitches. (b) Sweep over height and capillary pressure, with $d = 10$ μm and $l = 30$ μm constant. Taller pillars had a lower h_e that became increasingly invariant to interface shape. The last point of each curve represents the dryout condition for $\theta_{rec} = 15°$.

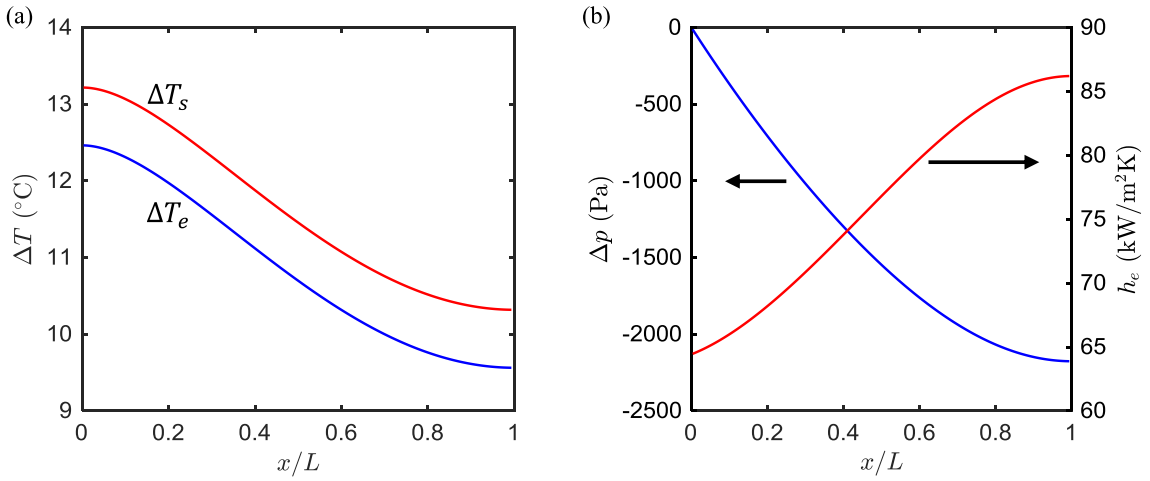

Fig. 4. Device simulation with $d = 10$ μm, $l = 30$ μm, $h = 25$ μm, $L = 5$ mm, and $q''_{in} = 82$ W/cm^2 in a vapor ambient at $T_{sat} = 100$ °C. (a) Distributions of evaporator (ΔT_e) and source (ΔT_s) superheat when the substrate thickness was 100 μm. ΔT_e was ~3 °C higher at the inlet than the center of the device. (b) Capillary pressure and h_e at position x/L relative to the liquid supply. h_e was directly calculated from Δp using the parametric study results. For the specified conditions, h_e varied ~30% across the evaporator surface.

3.3. Optimization

We used this model to compare dryout heat flux and HTC for various geometries to demonstrate its potential as an optimization tool. For this study, we considered a wick of standard microprocessor dimensions ($L = 5$ mm and $t_s = 100$ μm) with the receding contact angle for water on silicon dioxide ($\theta_{rec} = 15°$) in a pure water vapor ambient at T_{sat} = 100 °C. As in the previous section, only the sides of the wick normal to the x axis contacted the liquid supply (Fig. 1(c)) and the input heat flux was uniform. We varied h from 5 μm to 50 μm while maintaining $d/h = 0.4$ and $l/h = 1.2$ according to geometric ratios that Zhu et al. [14] reported as optimal for dryout heat flux. q''_{dryout} was determined by solving for the minimum heat flux at which Δp_{dryout} was reached on the wick. Fig. 5 shows the effect of increasing h on $\bar{h}_e$ and q''_{dryout}, where $\bar{h}_e$ is the average heat transfer coefficient on the wick at dryout conditions. For improved accuracy, q''_{dryout} was first calculated for uniform evaporation and the result was then used for the parametric study as q''_{in}, thus capturing any temperature dependence of h_e. The device-level model was iterated once more—now accounting for non-uniform evaporative flux—to determine $\bar{h}_e$ and q''_{dryout}. As h increased, q''_{dryout} increased monotonically, scaling with h^2. The dryout heat flux is enhanced by taller micropillars since the wick becomes more permeable, thus lowering the viscous resistance to capillary pumping. The permeability increases since fluid further from the no slip surface experiences weaker viscous effects. Conversely, $\bar{h}_e$ decreased with micropillar height because conduction resistance grows with film thickness. Since our model is capable of quantifying this tradeoff, it can be used in design optimization schemes that consider dryout and temperature. In contrast to prior studies that provided upper [21] and lower [18] bounds on HTC, our model resolves the distribution of HTC to obtain an accurate average corresponding to the specific conditions.

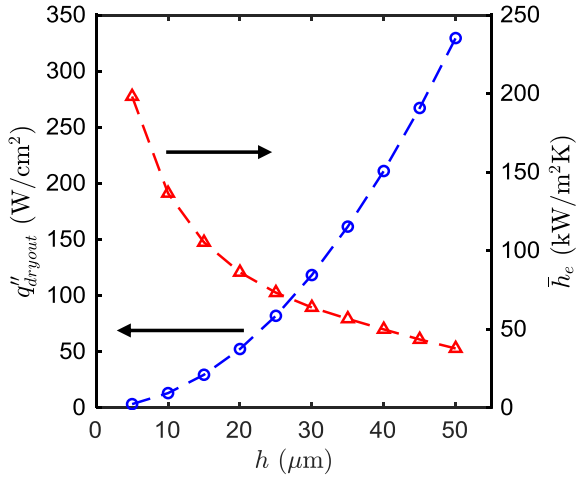

Fig. 5. Performance in terms of dryout and average HTC when micropillar height is varied. While previous models [12] have predicted the increase in q''_{dryout} with h, we now provide a comparison against the effect on $\bar{h}_e$. These results can be used to optimize wick design for both maximum heat load and temperature constraints. Each $\bar{h}_e$ was evaluated at the corresponding $q''_{in} = q''_{dryout}$ to account for temperature dependence. The geometric ratios were fixed at $d/h = 0.4$, $l/h = 1.2$ with wicking length $L = 5$ mm.

3.4. Model validation

Finally, we validated our model by comparing its $\bar{h}_e$ and q''_{dryout} results to previously reported experimental values. $\bar{h}_e$ was validated against work by Adera et al. [12], who measured heater temperature with a resistance temperature detector to monitor evaporator superheat. Their micropillar wick was placed in an environmental chamber at 3 kPa and surrounded by liquid water on all sides. They incrementally increased heat flux and reported superheat by assuming 1D conduction through the 650 μm thick silicon substrate. We first determined the accommodation coefficient $\alpha = 0.052$ by fitting to one set of data from [12] (*A1*) and then verified that our model matched well to their other data (*A2*) using the same value of α (Fig. 6(a)).

We compared q''_{dryout} to experiments by Zhu et al. [14] where one side of their micropillar wick was dipped into a water bath in an air ambient. Although the ambient being air rather than vapor greatly affects h_e, their experiment can validate the q''_{dryout} predicted by our present model since the ambient has little effect on dryout heat flux. This model accurately captured the trend shown by the experiments of q''_{dryout} to decrease as L increases (Fig. 6(b)).

4. Conclusions

We have formulated a comprehensive model for thin film evaporation in micropillar wicks that provides a complete understanding of performance in terms of three design criteria:

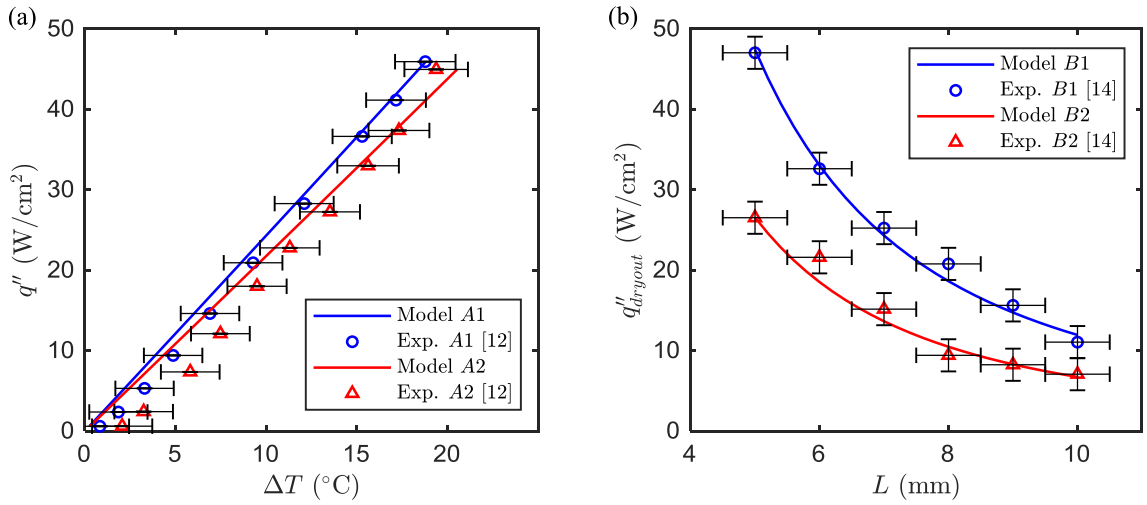

Fig. 6. Comparison to prior literature shows the model matches experimental data. (a) Superheat calculated by the model at various q''_{in} corresponding to experimental conditions from [12]. The accommodation coefficient was fit to *A1*. (b) Predicted dryout heat flux curves compared against experimental results from [14] over a range of wicking lengths. The device geometries (in μm) are *A1*: $d = 5$, $l = 12$, $h = 82$; *A2*: $d = 12$, $l = 20$, $h = 90$; *B1*: $d = 7$, $l = 20$, $h = 20$; *B2*: $d = 6$, $l = 50$, $h = 19$. Since the devices from [12] contacted the liquid reservoir on all sides, we accommodated for 2D flow in our fluid model for (a).

source temperature, evaporator temperature, and dryout heat flux. Whereas previous models are only capable of bounding the HTC, this work has fully resolved the local HTC, including the effects of both local curvature and micropillar geometry. Our model incorporates these curvature effects by coupling fluid flow and heat transfer to map distributions of HTC and temperature on the micropillar wick, giving the complete picture for evaporator performance. We have established the importance of our model by showing that the HTC can vary by ~30% over the evaporator surface and lead to inaccurate predictions with uniform HTC models. By identifying the location of the maximum temperature, we provide a means to efficiently mitigate boiling where the risk is highest. We characterized the tradeoff between dryout heat flux and HTC associated with film thickness, thus demonstrating a platform for comprehensive design optimization. Our model serves as a valuable tool to evaluate micropillar wicks for specific evaporator uses and has potential to guide design for other applications, such as wicking condensation [30]. Furthermore, our modeling approach can be applied generally to porous media with well-defined, periodic microstructure.

Conflict of interest

None declared.

Acknowledgments

The authors gratefully acknowledge funding from the National Science Foundation under Grant No. 1730389. We also thank Dr. Yangying Zhu at Stanford University and Dr. Solomon Adera at Harvard University for useful discussions.

Appendix A

A.1. Validation of assumptions

Our model operates under the following assumptions: a static normal stress balance (Eq. (2)) describes the interface, the rewetting flow is laminar, heat transfer in the liquid is purely by conduction, evaporation occurs in the near-equilibrium regime, and lateral heat conduction in the fluid is negligible. We demonstrate that these assumptions are valid using the following characteristic values: $l = h = 10$ μm, $L = 1$ cm, $q''_{in} = 100$ W/cm^2 (Fig. 1), and superheat $\Delta T = 10$ °C. All properties are evaluated for saturated water at 100 °C, the liquid phase is indicated by default unless the subscript "v" is used to denote vapor. Gravity and inertia have negligible effects on the interface shape compared to surface tension since the Bond ($Bo = \Delta\rho g l^2/\sigma \sim 10^{-5}$, where $\Delta\rho$ is the difference in density between the liquid and vapor phases, g is the acceleration due to gravity, and σ is the liquid-vapor surface tension) and Weber ($We = \rho u^2 l/\sigma \sim 10^{-2}$, where $u = q''_{in}L/(\rho h_{lv} h)$ and h_{lv} is the latent heat of vaporization) numbers are small. Curvature can be considered as constant in the unit cell if the viscous pressure drop over the cell is negligible compared to Laplace pressure, which is valid here since the Capillary number is small ($Ca = \mu u/\sigma \sim 10^{-3}$, where μ is the dynamic viscosity of the liquid). The rewetting flow is in the laminar regime since the Reynolds number $Re_h = \rho u h/\mu \sim 10^1$. Liquid velocity towards the interface ($u_e = q''_{in}/(\rho h_{lv})$) is slow enough that vertical convection can be neglected compared to conduction ($Pe_h = u_e h \rho c_p/k \sim 10^{-2}$, where k is the thermal conductivity of the liquid). Given that liquid enters the wick at T_{sat}, the low Jakob number ($Ja = c_p \Delta T/h_{lv} \sim 10^{-2}$, where c_p is the specific heat at constant pressure of the liquid) shows that liquid superheat is negligible, which is equivalent to negligible lateral convection. Therefore, only conduction must be considered. The Mach number of the vapor flow is sufficiently low ($Ma = u_v/\sqrt{\gamma R T_{sat}} \sim 10^{-3}$, where $u_v = q''_{in}/(\rho_v h_{lv})$ is the vapor speed, γ is the ratio of specific heats, and R is the specific gas constant) to be considered near-equilibrium. Finally, for the device shown in Fig. 4, the maximum temperature gradient between adjacent cells was 0.19% of the local gradient between the evaporator and ambient, verifying that symmetry conditions could be applied at lateral boundaries. Although the finite element nature of this model allows for simple integration of non-uniform heat loads (i.e., hotspots), accuracy of the symmetry assumption should be evaluated by comparing the lateral temperature gradient to superheat.

We neglect natural convection from the pillars according to an estimation of the resistance to natural convection (R_{nat}). Approximating the exposed pillar top as a flat plate, we have calculated R_{nat} from the Nusselt number correlation for low Rayleigh numbers and additionally have corrected for low Nusselt numbers as described in [31]. This method shows that R_{nat} is at least 2–3 orders

of magnitude higher than the interfacial resistance (R_{int}) to evaporation.

A.2. Mesh convergence

Mesh refinement studies were performed on all finite element calculations to quantify mesh independence of the results. To that end, we report mesh independence (Eq. (A1)) of a scalar variable Y as the relative difference between the result calculated on the mesh used in the study (Y_i) and that of a mesh with one additional degree of refinement (Y_{i+1}).

$$U_{relative} = abs\left(\frac{Y_{i+1}-Y_i}{Y_i}\right) \tag{A1}$$

Table A1
Representative mesh convergence statistics from the device simulation shown in Fig. 4.

Calculation	Parameter	DOF	$U_{relative}$
Interface shape	z_{min}	5551	1.1e−4
Cell HTC	h_e	21,904	1.4e−4
Cell permeability	κ	128,363	5.5e−4
Device flow	p_{min}	115	2.3e−6
Device conduction	$T_{max} - T_{min}$	809	9.9e−7

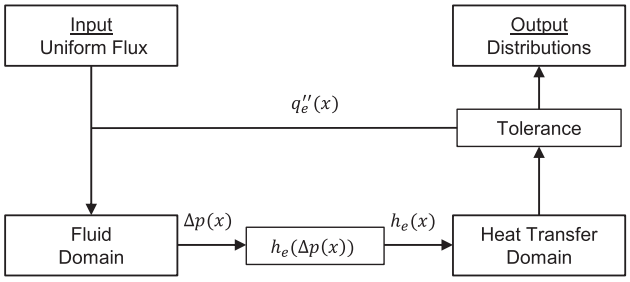

Fig. A1. Flow chart of the device-level model iterative approach. On the first iteration, uniform evaporative flux is assumed in the fluid domain, whereas subsequent iterations utilize the flux distribution. $\Delta p(x)$ and $q_e''(x)$ are passed back and forth between the fluid and heat transfer domains until a relative tolerance of 10^{-6} is met by the Euclidian norms of both $\Delta p(x)$ and $q_e''(x)$.

This analysis was applied to representative cases of each group of finite element calculation: interface shape, cell HTC, cell permeability, device-level Darcy flow, and device-level conduction. Table A1 lists the parameter evaluated, number of degrees of freedom (DOF) solved to determine Y_i, and $U_{relative}$ for the device simulated in Fig. 4. $U_{relative}$ is reported at the most extreme interfacial curvature (dryout conditions) for all parameters.

A.3. Iterative device-level model

We simulate micropillar wick performance by coupling fluid flow and heat transfer domains to account for the effects of local interfacial curvature. To achieve this coupling, we solve the distributions of pressure and evaporative heat flux using the iterative method depicted in Fig. A1. On the first iteration, the pressure distribution is calculated for a uniform evaporative flux where the local permeability is treated as pressure dependent and is solved using the lookup tables from the parametric study. The pressure distribution is then translated into a distribution of the heat transfer coefficient (again using the lookup tables), which is inputted to the heat transfer domain as a boundary condition. The heat transfer domain then calculates the temperature distribution and returns an updated heat flux distribution to the fluid domain for the next iteration. For all results presented in this paper, we cycled the iterative solver until the Euclidean norms of the pressure and heat flux distributions each converged to a relative tolerance of at most 10^{-6}.

A.4. Non-uniform heat loads

Since our model can resolve the distribution of HTC by accounting for local interfacial curvature, it is capable of accurately simulating device performance when the heat load is non-uniform. Although this capability is somewhat limited by the validity of the symmetry argument applied to the unit cell parametric study (see *A.1.*), it is nevertheless a valuable contribution of our modeling framework. We demonstrate this significance by considering a case where the micropillar wick received a high heat flux (100 W/cm^2) at a small "hotspot" while the remainder of the wick received a smaller (50 W/cm^2) background flux (Fig. A2). The peak temperatures were lower when the hotspot was located at the center of the wick (Fig. A2(a)) than when the hotspot was shifted to the inlet

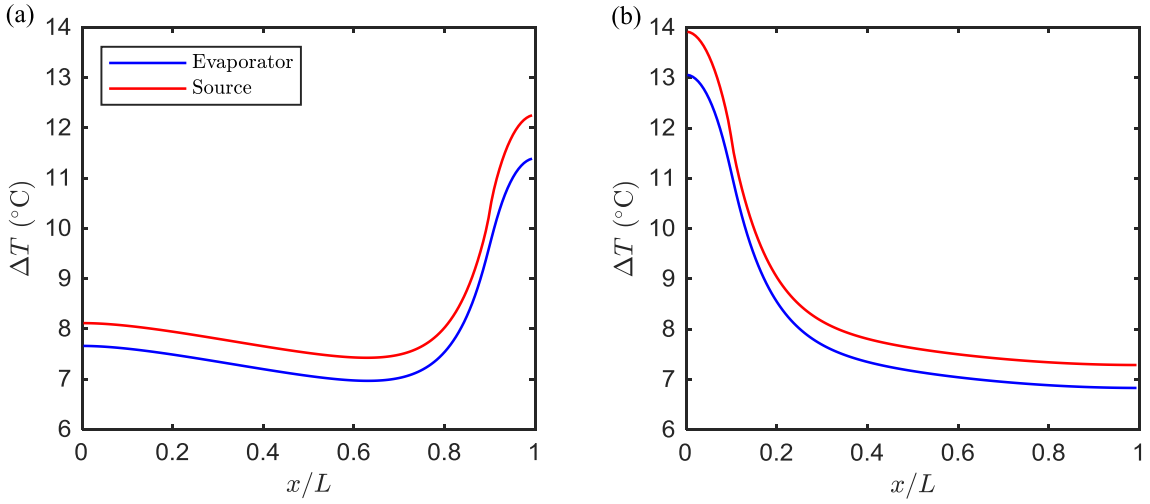

Fig. A2. Distributions of superheat obtained from simulations of the same device geometry as the results in Fig. 4 with a non-uniform heat load. (a) Heat load $q_{in}'' = 50$ W/cm^2 on $0 \le x/L \le 0.9$ and $q_{in}'' = 100$ W/cm^2 on $0.9 < x/L \le 1$. Unlike Fig. 4 (a), the maximum temperatures occurred at the center of the wick due to the localized heat flux. (b) Heat load $q_{in}'' = 100$ W/cm^2 on $0 \le x/L \le 0.1$ and $q_{in}'' = 50$ W/cm^2 on $0.1 < x/L \le 1$. For the same dimension and strength of the "hotspot," the micropillar wick maintained lower peak temperatures when the hotspot was placed at the center of the wick where the HTC was highest.

(Fig. A2(b)) due to favorable concentration of heat flux where the HTC was highest (as a result of curvature effects). Previous models that only consider upper/lower bounds of the HTC [18,21] cannot adequately describe device performance under non-uniform heat loads because they cannot capture the dependence on input heat flux distribution, i.e. hotspot location as shown in Fig. A2. Further, dryout heat flux is typically defined only for uniform heat flux [12,14], whereas the model presented here can determine the dryout condition for arbitrary heat loads since it resolves the pressure distribution. We quantified the validity of the symmetry argument for the device in Fig. A2(a) by calculating that the maximum temperature gradient between adjacent cells was 1% of the local gradient between the evaporator and the vapor ambient.

References

[1] E. Pop, Energy dissipation and transport in nanoscale devices, Nano Res. 3 (2010) 147–169.
[2] R. Mahajan, C.P. Chiu, G. Chrysler, Cooling a microprocessor chip, Proc. IEEE 94 (2006) 1476–1485.
[3] A. Majumdar, Thermoelectric devices: helping chips to keep their cool, Nat. Nanotechnol. 4 (2009) 214–215.
[4] J.R. Thome, The new frontier in heat transfer: microscale and nanoscale technologies, Heat Transf. Eng. 27 (2006) 1–3.
[5] Y. Zhu, D.S. Antao, D.W. Bian, S.R. Rao, J.D. Sircar, T. Zhang, E.N. Wang, Suppressing high-frequency temperature oscillations in microchannels with surface structures, Appl. Phys. Lett. 110 (2017).
[6] F. Yang, X. Dai, Y. Peles, P. Cheng, J. Khan, C. Li, Flow boiling phenomena in a single annular flow regime in microchannels (I): characterization of flow boiling heat transfer, Int. J. Heat Mass Transf. 68 (2014) 703–715.
[7] S.G. Kandlikar, History, advances, and challenges in liquid flow and flow boiling heat transfer in microchannels: a critical review, J. Heat Transfer. 134 (2012) 034001.
[8] J.A. Weibel, S.V. Garimella, M.T. North, Characterization of evaporation and boiling from sintered powder wicks fed by capillary action, Int. J. Heat Mass Transf. 53 (2010) 4204–4215.
[9] R. Xiao, S.C. Maroo, E.N. Wang, Negative pressures in nanoporous membranes for thin film evaporation, Appl. Phys. Lett. 102 (2013) 1–5.
[10] Z. Lu, T.R. Salamon, S. Narayanan, K.R. Bagnall, D.F. Hanks, D.S. Antao, B. Barabadi, J. Sircar, M.E. Simon, E.N. Wang, Design and modeling of membrane-based evaporative cooling devices for thermal management of high heat fluxes, IEEE Trans. Components, Packag. Manuf. Technol. 6 (2016) 1058–1067.
[11] M. Bulut, S.G. Kandlikar, N. Sozbir, A review of vapor chambers, Heat Transf. Eng. (2018) 1–23.
[12] S. Adera, D. Antao, R. Raj, E.N. Wang, Design of micropillar wicks for thin-film evaporation, Int. J. Heat Mass Transf. 101 (2016) 280–294.
[13] R. Ranjan, J.Y. Murthy, S.V. Garimella, A microscale model for thin-film evaporation in capillary wick structures, Int. J. Heat Mass Transf. 54 (2011) 169–179.
[14] Y. Zhu, D.S. Antao, Z. Lu, S. Somasundaram, T. Zhang, E.N. Wang, Prediction and characterization of dry-out heat flux in micropillar wick structures, Langmuir 32 (2016) 1920–1927.
[15] S. Adera, D.S. Antao, R. Raj, E.N. Wang, Hotspot thermal management via thin-film evaporation—Part II: Modeling, IEEE Trans. Components Packag. Manuf. Technol. 8 (2018) 99–112.
[16] Y. Nam, S. Sharratt, C. Byon, S.J. Kim, Y.S. Ju, Fabrication and characterization of the capillary performance of superhydrophilic Cu micropost arrays, J. Microelectromech. Syst. 19 (2010) 581–588.
[17] C. Byon, S.J. Kim, The effect of meniscus on the permeability of micro-post arrays, J. Micromech. Microeng. 21 (2011).
[18] M. Wei, B. He, Q. Liang, S. Somasundaram, C.S. Tan, E.N. Wang, Optimization and thermal characterization of uniform silicon micropillar based evaporators, Int. J. Heat Mass Transf. 127 (2018).
[19] R. Xiao, R. Enright, E.N. Wang, Prediction and optimization of liquid propagation in micropillar arrays, Langmuir. 26 (2010) 15070–15075.
[20] H.C. Brinkman, A calculation of the viscous force exerted by a flowing fluid on a dense swarm of particles, Appl. Sci. Res. 1 (1949) 155–161.
[21] S. Somasundaram, Y. Zhu, Z. Lu, S. Adera, H. Bin, W. Mengyao, C.S. Tan, E.N. Wang, Thermal design optimization of evaporator micropillar wicks, Int. J. Therm. Sci. 134 (2018) 179–187.
[22] R.W. Schrage, A Theoretical Study of Interphase Mass Transfer, Columbia Press, 1954.
[23] Z. Lu, D.J. Preston, D.S. Antao, Y. Zhu, E.N. Wang, Coexistence of pinning and moving on a contact line, Langmuir 33 (2017) 8970–8975.
[24] M.P. Do Carmo, Differential Geometry of Curves and Surfaces, Prentice Hall, Englewood Cliffs, NJ, 1976.
[25] COMSOL Multiphysics® v. 5.3a. www.comsol.com. COMSOL AB, Stockholm, Sweden, 2018.
[26] Y. Sone, Kinetic theoretical studies of the half-space problem of evaporation and condensation, Transp. Theory Stat. Phys. 29 (2000) 227–260.
[27] R. Meland, A. Frezzotti, T. Ytrehus, B. Hafskjold, Nonequilibrium molecular-dynamics simulation of net evaporation and net condensation, and evaluation of the gas-kinetic boundary condition at the interphase, Phys. Fluids. 16 (2004) 223–243.
[28] R. Meland, T. Ytrehus, Evaporation and condensation Knudsen layers for nonunity condensation coefficient, Phys. Fluids. 15 (2003) 1348–1350.
[29] R. Raj, S.C. Maroo, E.N. Wang, Wettability of graphene, Nano Lett. 13 (2013) 1509–1515.
[30] D.J. Preston, K.L. Wilke, Z. Lu, S.S. Cruz, Y. Zhao, L.L. Becerra, E.N. Wang, Gravitationally driven wicking for enhanced condensation heat transfer, Langmuir 34 (2018) 4658–4664.
[31] J.H. Lienhard IV, J.H. Lienhard V, A Heat Transfer Textbook, 4th ed., 2012.